ResearchGate

See discussions, stats, and author profiles for this publication at: https://www.researchgate.net/publication/325707043

Characterization of the Interface of an Alloy 625 Overlay on Steels Using Nanoindentation

Article *in* Journal of Materials Engineering and Performance · June 2018

DOI: 10.1007/s11665-018-3444-1

CITATIONS
0

READS
48

2 authors, including:

Tao Dai
The Ohio State University
11 PUBLICATIONS **26** CITATIONS

SEE PROFILE

Some of the authors of this publication are also working on these related projects:

Effect of Postweld Heat Treatment on the Properties of Steel Clad with Alloy 625 for Petrochemical Applications View project

All content following this page was uploaded by Tao Dai on 21 June 2018.

The user has requested enhancement of the downloaded file.

JMEPEG
https://doi.org/10.1007/s11665-018-3444-1
©ASM International
1059-9495/$19.00

Characterization of the Interface of an Alloy 625 Overlay on Steels Using Nanoindentation

Tao Dai and John Lippold

(Submitted December 12, 2017; in revised form March 9, 2018)

Industry standards require postweld heat treatment (PWHT) to reduce the heat-affected zone hardness of steels such as F22 (2.25Cr-1Mo) and AISI 8630 overlaid (clad) with Alloy 625 weld metal. PWHT results in carbon diffusion and accumulation at the interface between the steel and overlay. The accumulation of carbon in a planar solidification growth zone adjacent to the fusion boundary results in high hardness and the potential for hydrogen-assisted cracking. The planar growth zone (PGZ) is so narrow that normal Vickers hardness testing cannot fully reveal the hardness distribution in this zone. This study focused on the application of nanoindentation to characterize the hardness in the narrow microstructural regions adjacent to the fusion boundary. The development of nanohardness maps revealed that the PGZ is not necessarily the region that exhibits peak hardness after PWHT. The highest hardness values were associated with clusters of M_7C_3 carbides in specific subregions in the PGZ and also in the partially-mixed zone adjacent to the fusion boundary or in steel "swirl" structures. It was also confirmed in this study that nanohardness has a linear correlation with Vickers hardness values. The results presented here provide new insight into the role of carbon diffusion during PWHT and its effect on interface embrittlement associated with Alloy 625 overlays on steel.

Keywords alloy 625 overlay, joining, microscopy, nanoindentation, optical metallography, postweld heat treatment, steel, welding

1. Introduction

Overlaying (or cladding) low-carbon alloy steels with corrosion-resistant alloys (CRAs) such as Ni-based alloys or stainless steels is widely used in the oil and gas industry to provide corrosion protection. In certain situations, the fusion boundary of the dissimilar metal weld overlay is exposed to the production fluid, and the "sour" environments introduce the risk of sulfide stress cracking. In order to prevent this form of cracking, the heat-affected zone (HAZ) hardness must be controlled below 250 VHN according to National Association of Corrosion Engineers (NACE) Standard MR0175 and the International Standards Organization (ISO) 15,156 (Ref 1). PWHT is commonly applied to reduce the HAZ hardness, but this heat treatment results in carbon diffusion from the HAZ into the overlay. Previous research has shown that carbon diffusion and pileup can result in very high hardness in the planar solidification growth zone adjacent to the fusion boundary (Ref 2).

The planar growth zone (PGZ) is normally very narrow (10-50 μm) when examined in cross section which makes it difficult to determine the precise hardness using the Vickers hardness testing method, because the impression created by Vickers hardness testing with 100 g load possibly samples larger microstructural zones than narrow PGZ. A low-angle microsectioning technique has been used by previous researchers to expand the PGZ of 8630/625 overlay samples, revealing high hardness levels using Vickers hardness mapping (Ref 2). However, this method possibly does not reveal the true hardness distribution since the very low angle (7°-10°) results in very thin layers of both base metal and weld metal. In this case, the hardness indentation may penetrate into both layers and potentially not measure the actual hardness of the interface. As determined recently when evaluating the effect of PWHT on F22/625 and 8630/625 overlay samples, the actual hardness in the PGZ cannot be revealed until extreme PWHT conditions are used, e.g., 660 °C/100 h for F22/625 and 660 °C/50 h for 8630/625 overlay samples (Ref 3, 4). The use of nanoindentation provides a potential solution to this problem.

Nanoindentation was introduced by Oliver and Pharr in 1992 to measure hardness and elastic modulus (Ref 5). The mechanical properties can be calculated directly from the indentation load and displacement, with no requirement to view or measure the dimension of the indent (Ref 6). Nanoindentation has been applied in characterization of different materials and crystallographic phases, as well as the study of the interaction and properties of the interphase regions (Ref 7, 8). Characterization of the mechanical properties of the grain and grain boundaries using nanoindentation is also possible (Ref 8). Dodge used nanoindentation to study an area 60 μm × 60 μm across the fusion boundary of 8630/625 overlay samples, but he neither plotted the hardness map nor correlated the hardness distribution to the specific microstructure (Ref 9).

The use of nanoindentation to study dissimilar metal welds between steel and Ni-based filler metals is seldom reported. In this paper, the application of nanoindentation on both F22/625 and 8630/625 overlay welds is used to reveal the complex metallurgical reactions in the narrow regions adjacent to the fusion boundary. Both nanohardness line scans and nanohardness maps were generated in the regions adjacent to the fusion boundary. The hardness distribution of specific microstructures was revealed with the help of color etching and optical metallography. Nanoindentation and Vickers hardness testing were also compared, and a correlation relationship between the two methods is provided.

Tao Dai and **John Lippold**, Materials Science and Engineering, Welding Engineering Lab, Ohio State University, Columbus, USA. Contact e-mails: daitao11@gmail.com, dai.234@osu.edu.

Published online: 11 June 2018

2. Experimental Methods

2.1 Materials

Both the F22 steel and AISI 8630 steel were in the form of forged pipe sections. The diameter and nominal wall thickness of F22 steel pipe are 11.25 inch (285.8 mm) and 2.50 inch (63.5 mm), respectively. The diameter and nominal wall thickness of 8630 steel pipe are 11 inch (279.4 mm) and 2.04 inch (51.8 mm), respectively. Alloy 625 (AWS ERNiCrMo-3) was clad on the cross-sectional surfaces of the two pipes (Fig. 1a and b) using the hot-wire gas tungsten arc welding (HW-GTAW) process, and the bead stacking sequence with step distance of 0.15 inch (3.81 mm) is shown in Fig. 1(c) (see Ref 3, 4 for details of the cladding process). Table 1 provides the composition of F22 steel, 8630 steel and Alloy 625 filler metal.

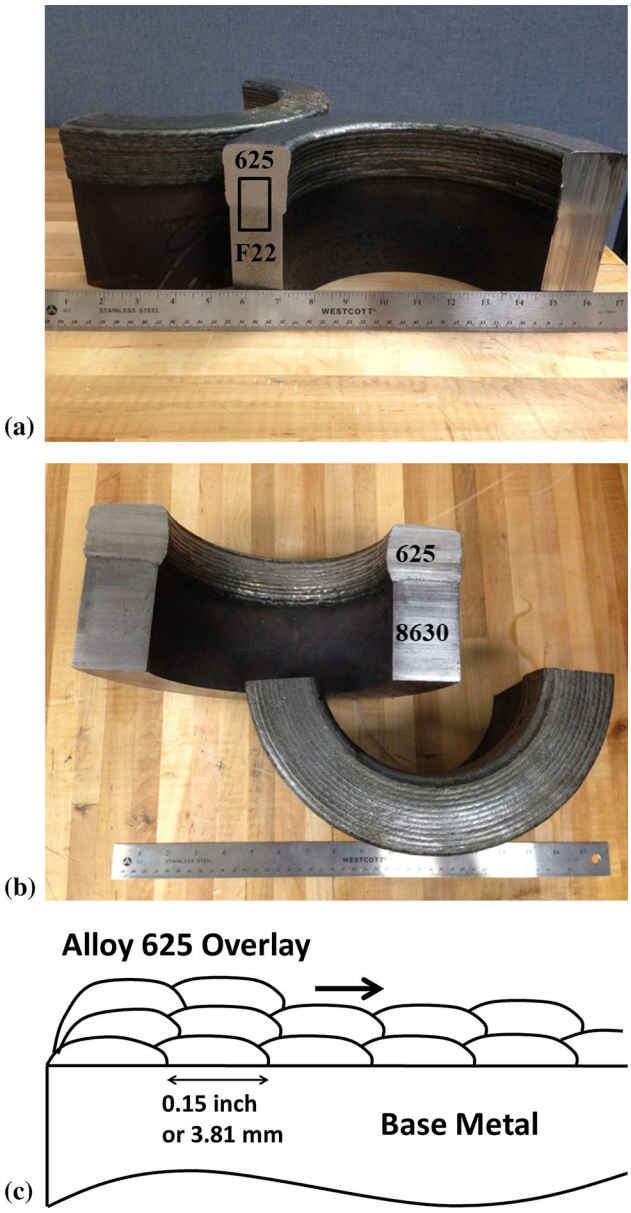

Fig. 1 Dissimilar metal weld coupons (a) F22/625, (b) 8630/625, (c) sketch of the bead stacking sequence

2.2 Postweld Heat Treatment

Postweld heat treatment (PWHT) was used to temper the steel HAZ following the cladding process. The degree of PWHT can be quantified using the Hollomon–Jaffe parameter (Ref 10), as shown in Eq 1. A wide range of PWHT conditions were studied in the previous work (Ref 3, 4), and based on this, two typical PWHT conditions were selected (Table 2) for nanoindentation studies of the F22/625 and 8630/625 overlay interfaces. The, respectively, selected PWHT conditions for two overlay samples can cause sufficient carbon diffusion from the base metal side to the weld metal side and pileup in a transition region adjacent to the fusion boundary. Thus, the hardness in the transition region is probably high.

$$\mathrm{HJP} = T(K) * (20 + \log t(hr)) \quad \text{(Ref 10)} \qquad \text{(Eq 1)}$$

2.3 Nanoindentation and Metallography

Nanoindentation was conducted using an MTS Nano Indenter® XP system to produce both nanohardness line scans and nanohardness maps. The system is extremely sensitive to vibration. The nanoindentation system is isolated using a minus k® vibration isolation table and thermal/sound insulated vibration isolation cabinet. Tip control mode was selected such that the indentation depth or penetration depth is a constant for all the nanoindentation, and as a result, the size and shape are the same for all the indents. In this work, 500 nm was selected as the penetration depth. For generating nanohardness line scans and maps, the distance between neighboring indents was selected as 6 μm. The maximum number of indents for a given hardness map was 400, which assured a hardness map with high resolution over an area that contained the weld interface regions of interest.

Metallographic cross sections of the weld interface were mounted in Bakelite™ and ground using sand paper #240, #400, #600 and #800. Then, the samples were polished with 6 and 1 μm diamond paste and finally polished manually using a 0.5-μm colloidal solution for 30 min. Samples used for nanoindentation cannot be etched since the etching will create an uneven sample surface and result in inaccuracy. To locate specific regions for nanoindentation, Vickers hardness indents were used to identify the target region.

For developing nanohardness maps, neighboring indents were spaced 6 μm on the x-axis and 10 μm on the y-axis. The nanohardness maps in this work contained either $20 \times 15 = 300$ or $20 \times 20 = 400$ indents. After nanoindenta-

Table 1 Chemical composition of base metals F22 steel, 8630 steel and filler metal Alloy 625

wt.%	C	Ni	Cr	Mn	Si	Mo	S	P	Al	Cu	Ti	Nb	V	Ta	Fe
BM F22	0.15	0.11	2.28	0.60	0.30	0.98	0.009	0.009	0.022	0.12	0.001	0.002	0.005	…	Bal.
BM 8630	0.32	0.86	0.97	0.90	0.32	0.41	0.009	0.008	0.026	0.17	0.002	…	0.032	…	Bal.
FM 625	< 0.01	64.0	22.7	< 0.01	0.04	9.0	0.001	< 0.011	0.12	< 0.011	0.23	3.59	…	0.004	0.3

Table 2 Selected PWHT conditions of F22/625 and 8630/625 overlay samples

	PWHT-1	PWHT-2
F22/625	660 °C/50 h (HJP = 20,154)	660°C/100 h (HJP = 20,526)
8630/625	650 °C/10 h (HJP = 19,383)	670°C/10 h (HJP = 19,803)

tion, the sample was etched with 5% Nital (5 vol.% nitric acid + 95 vol.% ethyl alcohol) to reveal the steel microstructure and then electrolytically etched in 10% chromic acid to reveal the weld metal microstructure (5.0 volts for 5 s). Metallographic images of the nanoindentation regions were located using the Vickers hardness indents. By overlaying the nanohardness lines and maps on corresponding indented regions, the nanohardness of specific microstructures at the weld interface was determined.

2.4 Conversion of Nanohardness to Vickers Hardness

Nanohardness is reported in terms of force (GPa) and is not readily convertible to other measures of hardness that are used in metallurgical studies. To date, there is no standard method to correlate nanohardness to Vickers hardness. In this work, an empirical method was used for this correlation. For each sample subjected to nanoindentation, 10-20 additional nanoindentations were made on both sides of the fusion boundary across the weld metal, HAZ and base metal to correlate with Vickers hardness. These indentations were spaced at ~ 100 μm. After nanoindentation, the sample was indented using Vickers hardness indenter in the same location of the nanoindentations, as shown in Fig. 2. By comparison, the nanoindentations are several microns in size compared to 20-30 μm for the Vickers hardness indents. The average of the nanohardness values versus the corresponding Vickers hardness value was then plotted to develop the correlation.

3. Results and Discussion

3.1 Single Nanoindentation

Figure 3(a) shows the variation of load as a function of displacement for a typical single nanoindentation on a F22/625 sample at PWHT 670 °C/10 h. The load increases up to ~ 30 mN until the displacement reaches the preset 500 nm and then decreases to ~ 2 mN. The decrease in displacement reflects the elastic "rebound" effect after the fixed penetration depth is reached. The modulus of the material can also be measured, and the modulus variation with the displacement is shown in Fig. 3(b). The load–displacement curve is typical of what is reported in other work, but the modulus–displacement data are seldom reported (Ref 6, 11, 12). In order to obtain a valid modulus–displacement curve, the penetration depth cannot be too small since a stable value is not achieved until the penetration is greater than 100 nm. The variation of the modulus in the depth range 300-400 μm indicates the inhomogeneity of the material (Fig. 3b). The nanoindents were compared with the Vickers hardness indents shown in Fig. 3(c). Though the penetration depth of the nanoindentation is 500 nm (0.5 μm), the surface dimension of the impression is about 3.7 μm due to the obtuse triangular Berkovich tip (Ref 11, 12).

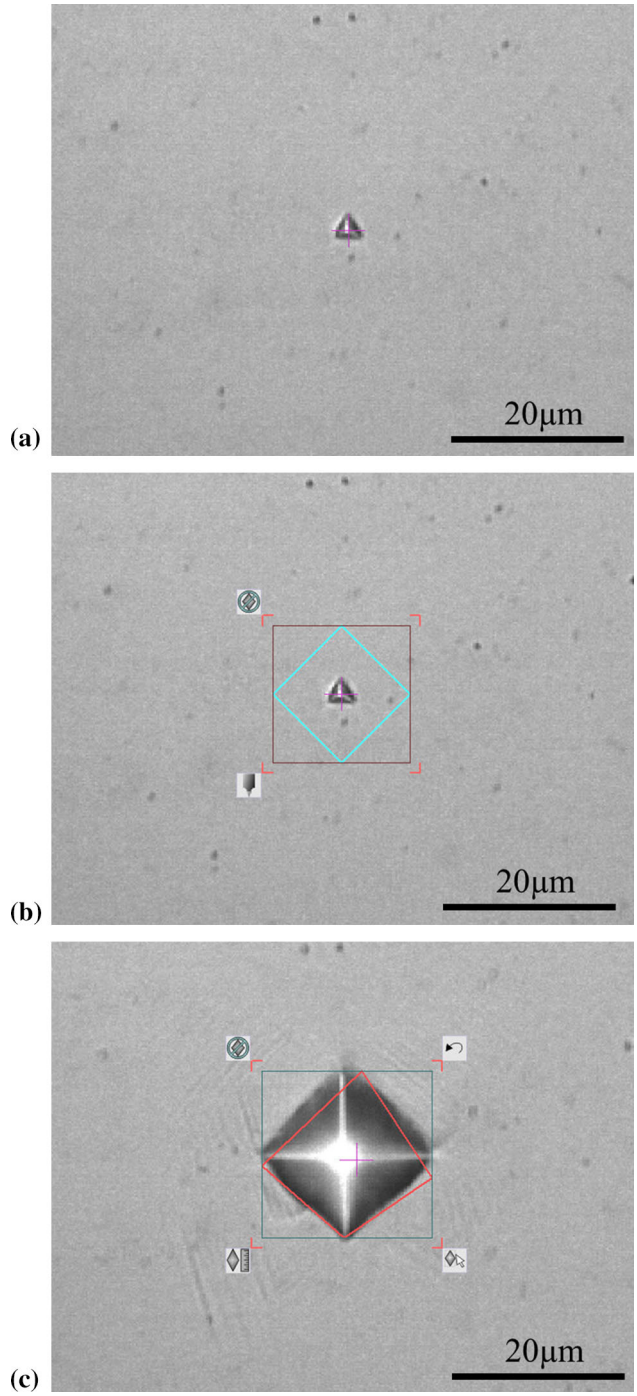

Fig. 2 Method to correlate the Vickers hardness with nanohardness at the same location, (a) nanoindentation, (b) locating the Vickers hardness indentation on the nanoindent, (c) Vickers hardness indentation after hardness measurement

3.2 Correlation Between Nanohardness and Vickers Hardness

The correlation between the nanohardness and Vickers hardness appears to be linear, as shown in Fig. 4. The VHN values converted from the nanohardness measurements tend to be larger than the actual Vickers hardness measurements (Ref 3, 4). This results from an indentation size effect, where the smaller nanoindenter is influenced more by the hard oxide layer with higher stiffness on the sample surface (Ref 13). With lower loads and shallower penetration, the higher is the fraction of elastic penetration coming from the hard oxide layer. The observed nanoindent size was left after the recover of the elastic penetration of the hard oxide layer (Ref 13). Thus, the hardness value measured by smaller indentation load is higher than that by larger indentation load.

Vickers hardness measured with a pyramidal diamond indenter and nanohardness with a Berkovich indenter are calculated using Eq 2 and 3, respectively (Ref 12). Two hardness values obviously have the same fundamental unit. Vickers hardness and nanohardness both represent the resistance of the material to plastic deformation on the sample surface. Therefore, it is expected that Vickers hardness and nanohardness would have a simple linear relationship, as has been reported by others (Ref 14-17).

$$\mathrm{HV} = \frac{F}{A_\mathrm{p}} = F/\left(\frac{d^2}{2\sin(136^\circ/2)}\right) \approx 1.8544F/d^2 \quad \text{(Ref 12)}, \tag{Eq 2}$$

$$H_\mathrm{n} = \frac{P}{A_\mathrm{c}} = P/24.5h_\mathrm{max}^2 \approx 0.00408P/h_\mathrm{max}^2 \quad \text{(Ref 12)}, \tag{Eq 3}$$

F and P are the pressure forces. A_p and A_c are, respectively, the projected areas in Vickers hardness test and the contact area in nanoindentation. d is the diagonal distance of the diamond-shaped Vickers hardness indent and h_max is the maximum penetration of the nanoindentation.

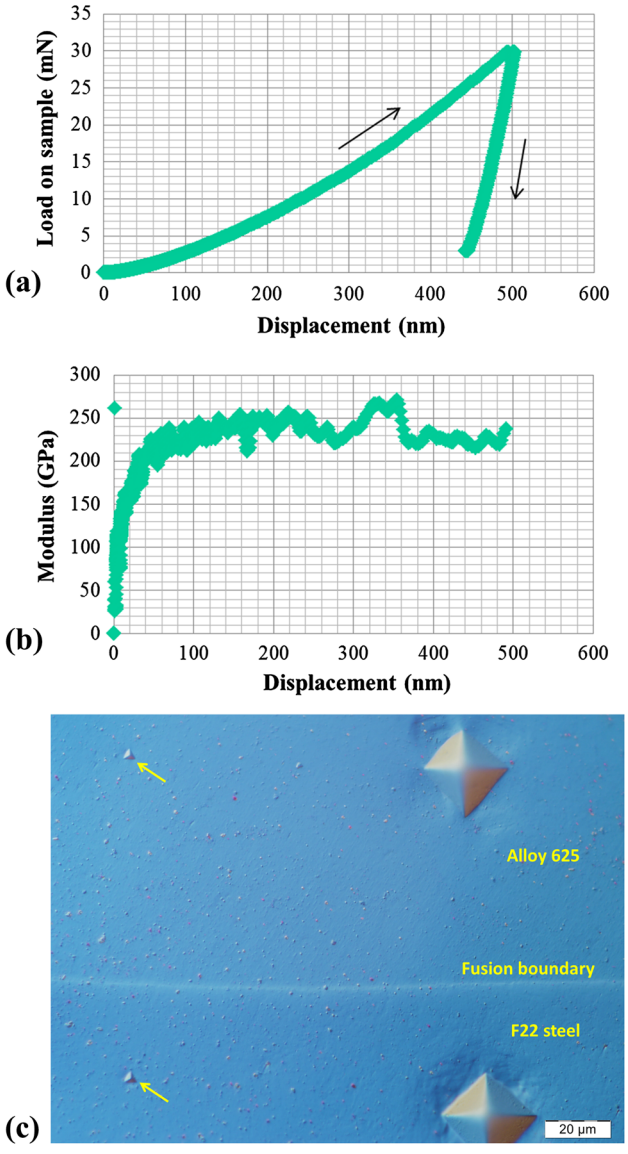

Fig. 3 Nanoindentation on F22/625 sample at PWHT 670 °C/10 h, (a) variation of load on sample with displacement, (b) variation of modulus with displacement and (c) dimension comparison between the nanoindents (arrows) and Vickers hardness indents

3.3 Nanohardness Line Scans

A nanohardness line scan is an important method to study the transition in properties across the fusion boundary of the dissimilar metal weld. After PWHT 670 °C/10 h on 8630/625 overlay sample, the hardness peaks at the interface can be clearly seen using nanoindentation as shown in Fig. 5. The hardness peaks are as high as 9.5 GPa, and the width of the high hardness region is about 20 µm. The Vickers hardness indentation cannot reveal the accurate hardness peak values because the dimension of Vickers hardness indent is about 20-30 µm when the applied load is 100 g. Vickers hardness line testing or Vickers hardness mapping can easily miss the narrow zone with high hardness at the interface, considering that the step distance between the Vickers hardness indents should be three times of the indent diameter. For Vickers hardness indentation with 100 g load, the distance is around 100 µm. Vickers hardness mapping on the F22/625 and 8630/625 overlay samples could not reveal the continuous hardness peaks along the fusion boundary even at extreme PWHT conditions (660 °C/100 h, HJP = 20,526) (Ref 3, 4).

In order to create a "wider" transition zone in the F22/625 and 8630/625 overlay samples, the low-angle microsectioning technique was used by previous researchers (Ref 2, 18).

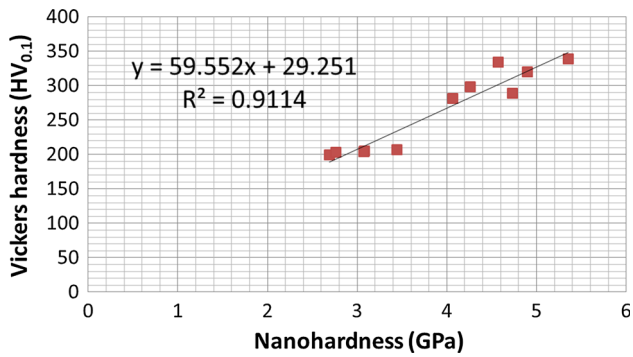

Fig. 4 Correlation between nanohardness and Vickers hardness in different regions of an F22/625 overlay sample tempered at 660 °C/50 h

Although effective in expanding this region, the fusion boundary became very irregular (curvy) making it difficult to determine the precise location of the interface. It is also difficult to perform SEM/EDX analysis on such irregular interfaces, making correlation between hardness and composition almost impossible. Vickers hardness measurements of the low-angle sections may be inherently inaccurate since the indent may penetrate through different regions not evident on the surface.

Using nanohardness line scans, most of the problems noted above can be eliminated. The resolution of the nanohardness line scan or map allows a "sharp" interface to be evaluated such that the fusion boundary separating the steel and weld metal is essentially perpendicular to the sample surface. Kim et al. (Ref 19) reported that the distance between neighboring indents has little effect on the measured hardness. Even when the distance is as small as an indent diameter, reliable hardness and elastic modulus values can be obtained. This is in contrast to the conventional view that sufficient distance (three indent diameters) between indents is needed to obtain reliable hardness values in microhardness testing. Thus, the step distance of 6 μm used in this work provides sufficient resolution to reliably measure the hardness variation in 20-30-μm-wide regions.

When overlaying the nanohardness line scan over the interface after etching, the nanohardness distribution in specific regions can be observed, as shown in Fig. 6 for two regions of an 8630/625 overlay at PWHT 650 °C/10 h. The interface or fusion boundary is indicated with yellow arrows. Figure 6(a) shows the nanohardness distribution from the 8630 HAZ (right) to the cellular solidification region, across the PGZ and the swirl structure. There is little hardness increase in the PGZ (or featureless zone) immediately adjacent to the fusion boundary (indicated with an orange arrow), but a hardness peak as high as 9.1 GPa was found in a narrow partially-mixed zone just to the right side of the swirl (indicated with a green arrow). The term partially-mixed zone was also used by Fenske and this zone was found to contain virgin martensite (Ref 20). The partially-mixed zone is of great interest due to its high hardness, and it was also found in many other samples at different PWHT conditions. Using Vickers hardness, such a narrow hard zone (5-10 μm) cannot be detected. The etching procedure reveals that this partially-mixed zone consists of a fine lath- or needle-like structure. This confirmed Fenske's result (Ref 20) that the partially-mixed zone consists of virgin martensite that is potentially susceptible to hydrogen-assisted cracking (HAC) and sulfide stress cracking (SSC).

Another interesting finding is that a high hardness peak is present just at the brownish features in the PGZ of the 8630/625 samples after PWHT, as shown in Fig. 6(b) (indicated with blue arrows). Fenske and Dodge found M_7C_3 carbides in the PGZ

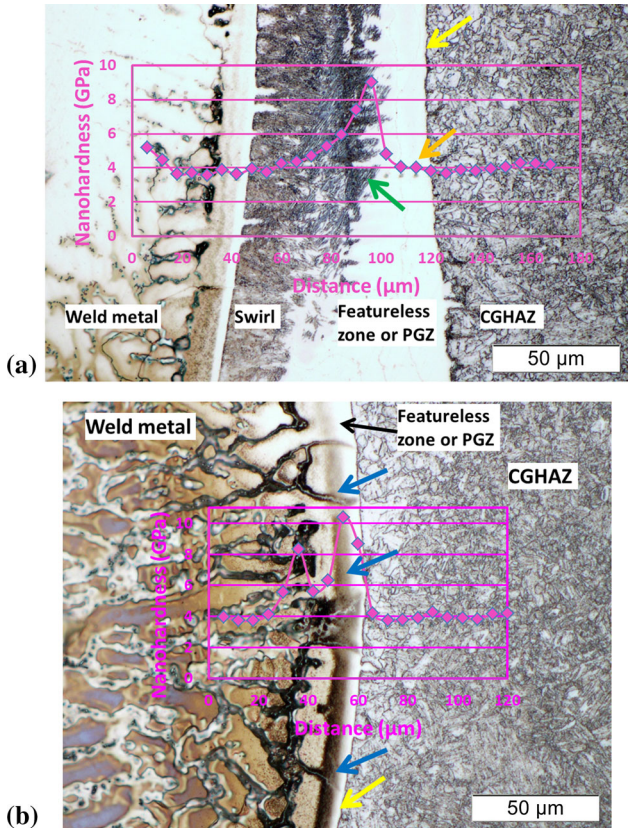

Fig. 6 Nanohardness line scans across the fusion boundary of 8630/625 overlay samples tempered at 650 °C/10 h (a) fusion boundary with a swirl structure. The green arrow indicates the partially-mixed zone, and the yellow arrow indicates the fusion boundary. (b) Fusion boundary without a swirl structure. The blue arrows indicate the brownish features, and the yellow arrow indicates the fusion boundary (Color figure online)

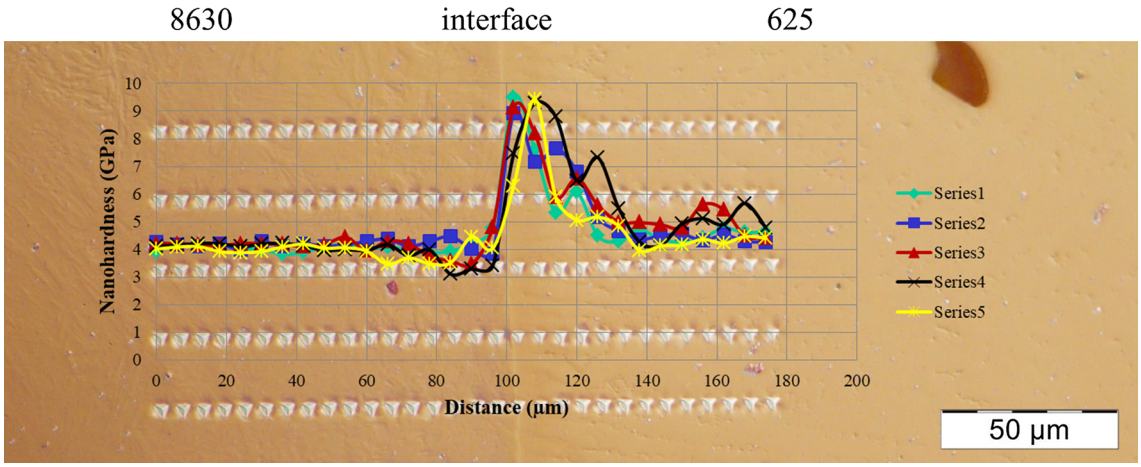

Fig. 5 Five nanohardness line scans across the fusion boundary of 8630/625 at PWHT 670 °C/10 h

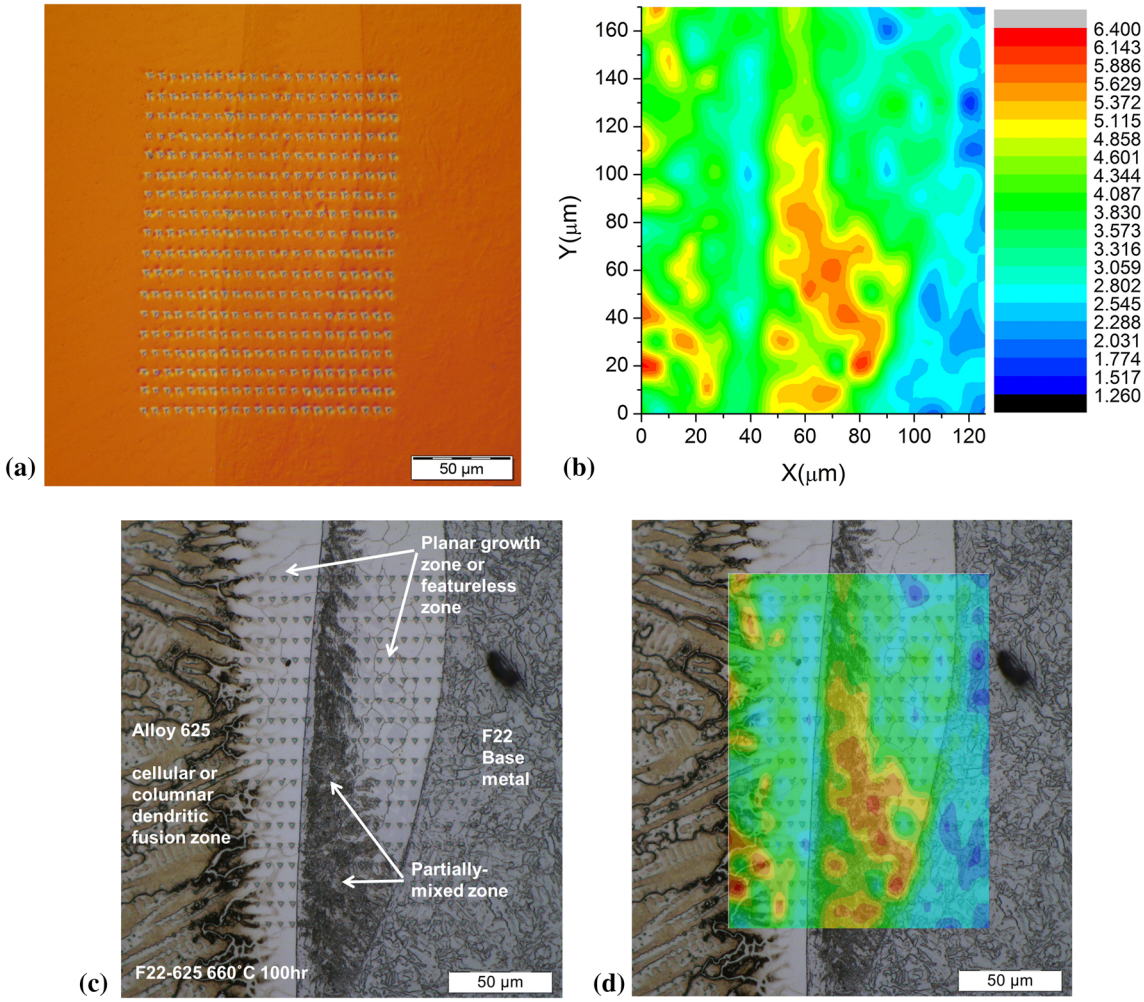

Fig. 7 Nanohardness map of F22/625 sample tempered at 660 °C/100 h, (a) 22 × 15 matrix of nanohardness indents, (b) nanohardness map, (c) microstructure of the indented region and (d) nanohardness map overlaid on the microstructure (Color figure online)

when the 8630/625 overlay samples were tempered at 650 °C/10 h or at more severe PWHT conditions (Ref 9, 20). Dodge also found a 2-3-μm-wide precipitate-free zone in the PGZ immediately adjacent to the fusion boundary (Ref 9). This occurs because carbon diffuses a short distance into the PGZ before carbide precipitates start to form, which occurs about 2-3 μm away from the fusion boundary, rather than immediately adjacent to the boundary. This precipitation is consistent with the position of brownish features (Fig. 6b), which are also not immediately adjacent to the fusion boundary, which is indicated with a yellow arrow in Fig. 6(b). Therefore, the brownish features shown in Fig. 6(b) represent clusters of M_7C_3 carbides which result in local hardening. This explains specifically why the hardness in the PGZ increases after PWHT, rather than simply describing that hardness peaks due to carbon diffusion and pileup in the transition zone (Ref 2). This local hardening also explains the high HAC susceptibility of the PGZ after that extreme PWHT conditions are used to temper the HAZ of the steel (Ref 9, 20-22).

3.4 Nanohardness Mapping

Nanoindentation mapping can provide the hardness distribution of a small-scale microstructure at much higher resolution than possible using Vickers hardness mapping. Figure 7(a) shows a matrix of nanoindents at the fusion boundary of an F22/625 overlay sample at PWHT 660 °C/100 h. The analysis grid contains 22 ×15 = 330 indents. The neighboring indents distance is 6 μm and 10 μm in *x*-axis direction and *y*-axis direction, respectively. The nanoindent is an equilateral triangle with a lateral length ~ 3.7 μm by calculation based on the penetration depth and the geometry of the tip. Figure 7(b) shows the nanohardness map of the indents matrix in Fig. 7(a). The highest hardness is 6.420 GPa (in gray region of Fig. 7b), and the lowest is 1.260 GPa. After re-polishing and etching the indent region, the microstructure is shown in Fig. 7(c). Adjacent to the fusion boundary is the partially-mixed zone, which contains small lath structures and has high hardness. Thus, it is probably martensite as shown in Fig. 6(a). The A_3 temperature in this zone is probably lower than the PWHT temperature 660°C because of higher content of nickel, chromium and carbon. After quenching from PWHT temperature 660 °C to room temperature, the region transformed to martensite with fine lath structures.

After overlaying the nanohardness map on the microstructure, the hardness distribution of the region can be revealed at high resolution (Fig. 7d). The low nanohardness area (about 2.5-3.0 GPa) in blue exactly overlaps the steel HAZ. Across the fusion boundary, the nanohardness increases abruptly. The partially-mixed zone shows especially high nanohardness.

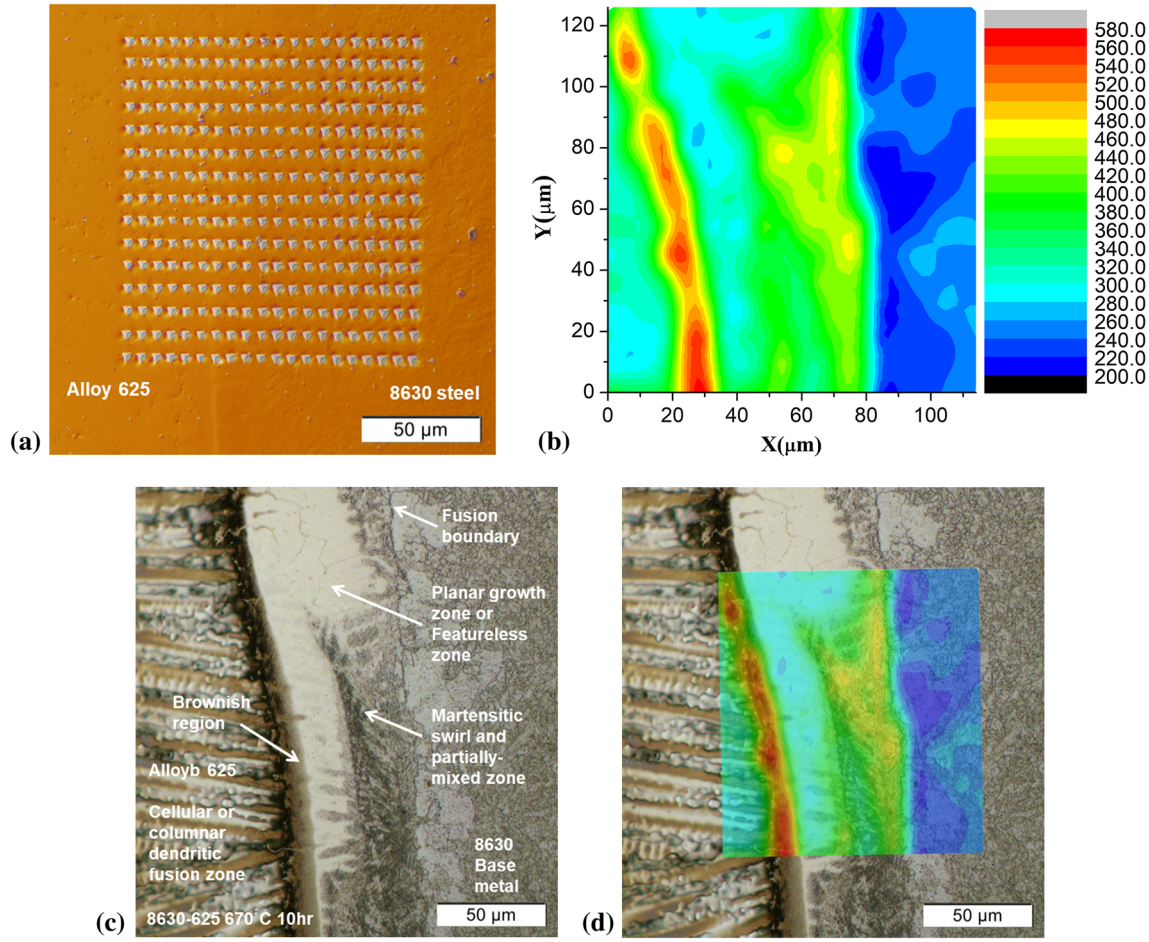

Fig. 8 Nanohardness map of 8630/625 sample tempered at 670 °C/10 h. (a) 20 × 15 matrix of nanohardness indents, (b) hardness map of the indents matrix after conversion of nanohardness to Vickers hardness, (c) microstructure of the indented region and (d) nanohardness map overlaid on the microstructure (Color figure online)

However, the PGZ or featureless zone does not exhibit high nanohardness as thought. In fact, the nanohardness in the PGZ is even lower than the cellular or columnar dendritic zone and only slightly higher than the base metal HAZ (Fig. 7d). The nanohardness in the cellular or columnar dendritic zone is inhomogeneous due to solidification segregation and subsequent precipitation during PWHT. Some regions are blue with nanohardness of 3.0-3.5 GPa, and others are red with the nanohardness greater than 6 GPa (Fig. 7d), but its most area is in green color with nanohardness of 4-5 GPa.

Similar to Fig. 7, Fig. 8 demonstrates the methodology for displaying the nanohardness distribution of a 8630/625 overlay sample tempered at 670 °C/10 h. Figure 8(a) shows a 20 × 15 matrix of nanoindents, which covers an area 120 μm × 150 μm. As compared to the required spacing between Vickers hardness indents, only one $HV_{0.1}$ indent could be made in such a small area and detailed hardness information as it relates to microstructure could not be obtained. Using the linear correlation between nanohardness and Vickers hardness, the nanohardness values were converted to Vickers hardness and are plotted in a map as shown in Fig. 8(b). In this small area across the fusion boundary, there is a wide range of hardness variation from 200 to 580 $HV_{0.1}$. The hardness distribution can be revealed clearly by overlaying the hardness map and the microstructure. In Fig. 8(c), the swirl and partially-mixed zone have tiny lath-like martensitic structures, with the hardness in the range of 340-480 $HV_{0.1}$, higher than that of the PGZ. The hardness of the PGZ is around 300 $HV_{0.1}$, higher than that of the CGHAZ or base metal (200-260 $HV_{0.1}$).

On the outer edge of the cellular region or the left edge of the featureless zone (Fig. 8c), there is a narrow region with brownish features where the hardness is above 500 $HV_{0.1}$. The brownish features are the same with that described in Fig. 6(b). As discussed previously, these are clusters of M_7C_3 carbides, and the local precipitation hardening results in a hardness peak. The PWHT condition 670 °C/10 h is so extreme for the 8630/625 overlay sample that the carbon was driven to diffuse across the PGZ and accumulated on the edge of the PGZ close to the cellular solidification region in Fig. 8(d). Thus, the hardness peaks are adjacent to the boundary between the featureless zone and the cellular region, rather than being adjacent to the fusion boundary.

4. Conclusions

This investigation shows that nanoindentation is a valuable tool to assist the microstructure characterization in the regions near the fusion boundary of dissimilar metal welds between Ni-based Alloy 625 and steels. The hardness information can help to determine microstructure type, and two examples are

illustrated in this work. The partially-mixed zone was found and confirmed to contain martensitic microstructure. The clusters of carbides precipitation were also determined with nanoindentation in the planar growth zone (PGZ) or featureless zone. These two microstructures with high hardness are potentially susceptible to hydrogen-assisted cracking or sulfide stress cracking. The previous general view is that during postweld heat treatment, carbon diffuses to the PGZ and piles up in this zone, leading to high hardness in the PGZ. Revealed with the combination of color-etching optical microscopy and nanohardness mapping, the PGZ does not necessarily have particularly high hardness. The hardness peaks are only at the location with carbides precipitation in the PGZ. It was confirmed that nanohardness and Vickers hardness ($HV_{0.1}$) have a linear correlation.

Acknowledgments

This work was supported by Schlumberger (originally Cameron International) through the NSF I/UCRC Manufacturing and Materials Joining Innovation Center (Ma^2JIC) at the Ohio State University. Cameron International provided the base materials, and Acute Technological Services provided the filler metal Alloy 625 and produced the overlay weld samples. The assistance of Andres Acuna for providing instruction on use of nanoindentation equipment is also appreciated.

References

1. NACE MR0175/ISO 15156-2: 2009, Petroleum and Natural Gas Industries-Materials for Use in H2S-Containing Environments in Oil and Gas Production-Part 2: Cracking-Resistant Carbon and Low Alloy Steels and the Use of Cast Iron. in *International Standard*, NACE International/ISO2001, 2003, pp. 17–44
2. B.T. Alexandrov, J.C. Lippold, J.W. Sowards, A.T. Hope, and D.R. Saltzmann, Fusion Boundary Microstructure Evolution Associated with Embrittlement of Ni-Base Alloy Overlays Applied to Carbon Steel, *Weld. World*, 2013, **57**, p 39–53
3. T. Dai and J.C. Lippold, Tempering Behavior of Fusion Boundary Region of Alloy 625 Weld Overlay on 2.25Cr-1Mo Steel, *Weld. J.*, 2017, **96**, p 467s–480s
4. T. Dai and J.C. Lippold, Tempering Behavior of the Fusion Boundary Region of Alloy 625 Weld Overlay on 8630 Steel, *Weld. World*, 2018, **62**, p 535–550
5. W.C. Oliver and G.M. Pharr, An Improved Technique for Determining Hardness and Elastic Modulus Using Load and Displacement Sensing Indentation Experiments, *J. Mater. Res.*, 1992, **7**(6), p 1564–1583
6. W.C. Oliver and G.M. Pharr, Measurement of Hardness and Elastic Modulus by Instrumented Indentation: Advances in Understanding and Refinements to Methodology, *J. Mater. Res. (JMR)*, 2004, **19**, p 3–20
7. W. Zhu, J.J. Hughes, N. Bicanic, and C.J. Pearce, Nanoindentation Mapping of Mechanical Properties of Cement Paste and Natural Rocks, *Mater. Charact.*, 2007, **58**, p 1189–1198
8. P. Maier, A. Richter, R.G. Faulkner, and R. Ries, Application of Nanoindentation Technique for Structural Characterisation of Weld Materials, *Mater. Charact.*, 2002, **48**, p 329–339
9. M.F. Dodge, *The Effect of Heat Treatment on the Embrittlement of Dissimilar Welded Joints—Dissertation*, University of Leicester, Leicester, UK, 2014
10. J. Hollomon and L. Jaffe, Time-Temperature Relations in Tempering Steel, *Met. Technol.*, 1945, **12**, p 223–249
11. D.A. Lucca, K. Herrmann, and M.J. Klopfstein, Nanoindentation: Measuring Methods and Applications, *CIRP Ann. Manuf. Technol.*, 2010, **59**, p 803–819
12. A.C. Fischer-Cripps, *Nanoindentation*, 3rd ed., Springer, New York, 2011
13. X. Shi, H. Yang, G. Shao, X. Duan, and Z. Xiong, Nanoindentation Study of Ultrafine WC–10Co Cemented Carbide, *Mater. Charact.*, 2008, **59**, p 374–379
14. P. Mencin, C.J. Van Tyne, and B.S. Levy, A Method for Measuring the Hardness and Elastic Modulus of the Surface Layer on Hot Forging Dies Using a Nano Indentation, *J. Mater. Eng. Perform.*, 2009, **18**(8), p 1067–1072
15. Rice, P.M., and Stoller, R.E., Correlation of Nanoindentation and Conventional Mechanical Property, in *MRS Online Proceeding Library Archive,* 2000, p. 649
16. Sawa, T., Correlation between Nanoindentation Test Result and Vickers Hardness, in *IMEKO 2010 TC3, TC5 and TC22 Conferences*, Pattaya, Chonburi, Thailand, 2010
17. Zhang, L., Ohmura, T., and Tsuzaki, K., Application of Nanoindentation Technique in Martensitic Structures, in *Nanoindentation in Materials Science*, InTech, 2012, pp. 109–130
18. D. Bourgeois, *Hydrogen Assisted Crack in Dissimilar Metal Welds for Subsea Service under Cathodic Protection: Dissertation*, The Ohio State University, Columbus, 2015
19. H.J. Kim and D.E. Kim, Effects of Proximity on Hardness and Elastic Modulus Measurements of SiO_2 and Cu by Nanoindentation, *Tribol. Lett.*, 2013, **49**, p 85–94
20. J.A. Fenske, *Microstructure and Hydrogen Induced Failure Mechanisms in Iron-Nickel Weldments*, University of Illinois at Urbana-Champaign, Urbana, IL, 2010
21. T. Dai and J.C. Lippold, The Effect of Postweld Heat Treatment on Hydrogen Assisted Cracking of F22/Alloy 625 Overlays, *Weld. J.*, 2018, **97**, p 75s–90s
22. Dai, T. and Lippold, J.C., The Effect of Postweld Heat Treatment on Hydrogen-Assisted Cracking of 8630/Alloy 625 Overlay, *Weld. World*, 2018, **62**, p 581–599

View publication stats